Atomic force microscopy of freeze-fracture replicas of rat atrial tissue

L. KORDYLEWSKI, D. SANER & R. LAL
University of Chicago, Department of Medicine/Cardiology, 5841 S. Maryland Ave., Chicago, IL 60637, U.S.A.

Summary

Atomic force microscopy (AFM) has provided three-dimensional (3-D) surface images of many biological specimens at molecular resolution. In the absence of spectroscopic capability for AFM, it is often difficult to distinguish individual components if the specimen contains a population of mixed structures such as in a cellular membrane. In an effort to understand the AFM images better, a correlative study between AFM and the well-established technique of transmission electron microscopy (TEM) was performed. Freeze-fractured replicas of adult rat atrial tissue were examined by both TEM and AFM. The same replicas were analysed and the same details were identified, which allowed a critical comparison of surface topography by both techniques. AFM images of large-scale subcellular structures (nuclei, mitochondria, granules) correlated well with TEM images. AFM images of smaller features and surface textures appeared somewhat different from the TEM images. This presumably reflects the difference in the surface sensitivity of AFM versus TEM, as well as the nature of images in AFM (3-D surface contour) and TEM (2-D projection). AFM images also provided new information about the replica itself. Unlike TEM, it was possible to examine both sides of the replica with AFM; the resolution on one side was significantly greater compared with the other side. It was also possible to obtain quantitative height information which is not readily available with TEM.

Introduction

Newly developed scanning probe microscopes are emerging as a powerful tool for imaging. The first of these, the scanning tunnelling microscope (Binnig & Rohrer, 1982), provides atomic resolution information on many structures that are electrically conducting (for reviews see Zasadzinski & Hansma, 1990; Engel, 1991). Though images of non-conducting biological specimens have been obtained, the mechanism(s) of image generation and their interpretation are unclear (Zasadzinski & Hansma, 1990; Clemmer & Beebe, 1991; Engel, 1991; Heckl & Binnig, 1992). More recently, Binnig et al. (1986) developed the atomic force microscope (also known as the scanning force microscope) which can obtain the three-dimensional (3-D) surface structure of biological specimens in a fluid environment (Marti et al., 1988; Rugar & Hansma, 1990; Lal & John, 1994).

Although the atomic force microscope can obtain molecular-resolution surface images of crystalline as well as amorphous materials (Butt et al., 1990; Hoh et al., 1991; Lal et al., 1993; Lal & Yu, 1993; Yang et al., 1993), it is often difficult to distinguish individual components if the surface contains a heterogeneous population of substructures, such as in a cellular membrane.

For a reliable application of atomic force microscopy (AFM) to biological imaging it is essential that the individual components in an image are unambiguously identified. During the early phase of AFM development, a critical comparison of information obtained from AFM and other established microscopic techniques, like electron microscopy (EM), could provide such unambiguous distinction. The importance of such a correlative study in the field of microscopy has been emphasized by Hayat (1987). A correlative study of the nuclear pore complex by AFM and EM has recently been reported (Pante & Aebi, 1993); however, these studies were not conducted on the same specimen.

The aim of the present study was to analyse the same specimen and its substructures with both TEM and AFM. Freeze-fracture replicas of biological specimens are often used for EM studies and have provided a wealth of knowledge regarding cellular and subcellular architecture (Kordylewski et al., 1983; Page et al., 1986; Roberts et al., 1991). Replicas have been imaged by STM (Zasadzinski et al., 1988) and are amenable to AFM imaging. We chose freeze-fracture replicas of rat atrial tissues for this study. These replicas were well characterized by TEM previously (Kordylewski et al., 1993).

AFM allowed examination of the same regions on both sides of the same replica. Large-scale features present in the TEM and AFM images appeared similar and were easy to correlate; however, fine details appeared dissimilar. Such dissimilarity presumably arose because AFM detects only 3-D surface details, whereas EM obtains images of variations in the bulk (as a 2-D projection). AFM images, in addition, provided a direct estimate of the height of the surface convolution (i.e. 3-D information) commonly unavailable with freeze-fracture EM studies (Hoppe, 1991; Turner, 1981; Engel et al., 1982; Kordylewski et al., 1983, 1985; Kordylewski & Florek, 1990). A better understanding of the nature of differences in AFM and TEM images of the same specimen may improve the understanding of the imaging artefacts of both microscopical techniques and provide a limit of confidence for the AFM imaging of complex biological specimens.

Methods

Replicas of rat atrial tissue were prepared as described by Kordylewski et al. (1985, 1993). These replicas were mounted on 400-mesh finder grids (H-7 London, Maxtaform Grids by Graticules, Ltd), and analysed and photographed in a Hitachi H-600 electron microscope in the TEM mode as described previously (Kordylewski et al., 1985, 1993). The electron microscope was equipped with a eucentric, side-entry goniometer stage that permitted tilting of the specimen for taking stereo pairs of the details examined. Stereo-pair photographs were taken at a tilt of $5°$ to each other (Kordylewski et al., 1983, 1985).

AFM images were obtained using a Nanoscope III AFM (Digital Instruments, Santa Barbara, CA) equipped with either a 13×13-μm or 120×120-μm stage. The stage was calibrated for height (z), using a 180-nm step height standard, and lateral measurement (x, y), on a diffraction grating, at Digital Instruments. Images were obtained using a V-shaped, 100-μm-long microfabricated Si_3N_4 cantilever with integrated tips of nominal spring constant $\sim 0\cdot38\,N/m$ (Digital Instruments). Due to the rigid nature of the specimen, it was not necessary to minimize the contact force during imaging. Indeed, the best quality images were obtained at a high imaging force ($\sim 30\,nN$). Various tests for artefacts, including rotation of scan direction with respect to images, effect of scan rate, effect of imaging force (set point force), and stability of images over multiple scans, were performed as previously described (Hoh et al., 1991; Lal et al., 1993; Lal & Yu, 1993; for a discussion of imaging artefacts see reviews by Engel, 1991; Lal & John, 1994).

Preliminary observations showed that AFM images obtained in 'error mode' (Putnam et al., 1992) were much easier to correlate with the TEM images. This is due to a shadowing effect created by the error-mode imaging which is visually similar to the shadowing effect produced in the TEM. With error-mode imaging, an image is reconstructed from the error signal of the feedback loop and actually represents the derivative of the surface convolution. Thus, when the tip encounters a bump on the surface, the rising side will appear light and the falling side dark. A similar effect can be produced off-line using standard height-mode data with simulated illumination. AFM images presented here are in either error mode or simulated illumination of the height-mode data.

Distances (both lateral and vertical) were measured using the program provided with the Nanoscope III software described previously (Hoh et al., 1991; Lal et al., 1993; Lal & Yu, 1993). For these measurements, the height-mode images were used since they provide the real height information; such information is ambiguous in error-mode imaging.

To protect the replicas from possible damage due to excessive electron beam exposure, some low-magnification panoramic views of the entire replicas were first taken in the EM. Subsequently, the specimen was imaged by AFM using the finder grid as a positional reference. The low-magnification EM images were helpful in locating specific specimen areas during AFM imaging, and for one-to-one correspondence of areas studied by both techniques. The replica was then transferred back to the electron microscope and the details previously imaged by AFM were identified and stereo-photographed at higher magnification.

Both sides of the replicas were examined by AFM. For the sake of clarity, the side of the replica which was exposed outward on the EM grid will be referred to as side A and the side facing the substrate (the EM grid) will be referred to as side B. It was possible to image side A with the sample still on the EM grid. As side B of the sample was orientated facing downward on the EM grid, it was necessary to turn the sample upside down so that side B was facing upward. As it turned out, the grid thickness ($\sim 30\,\mu$m, as cited by the manufacturer) and the size of the grid holes ($64 \times 64\,\mu$m) were such that the AFM tip ($\sim 10\,\mu$m in height, $\sim 22\,\mu$m wide, $100\,\mu$m long) could not make good contact with the sample through the grid. For this reason, the replicas were carefully removed from the EM grid so that side B remained unperturbed. This was accomplished by touching side A of the replica with a piece of double-sided sticky tape, gently removing the replica from the EM grid, and fixing the tape to an AFM sample holder. This procedure also improved imaging by AFM because the sample was more directly and rigidly attached to the sample holder. The replica was removed last, since it precluded the possibility of further study with the electron microscope.

Obtaining images from side A of the replica was considerably more difficult due to the lack of rigid mounting; the replica was held on the EM grid only by a weak adhesive force. Under a light microscope, the replica could often be seen to move as the tip scanned over a particular area. It would return to its original conformation
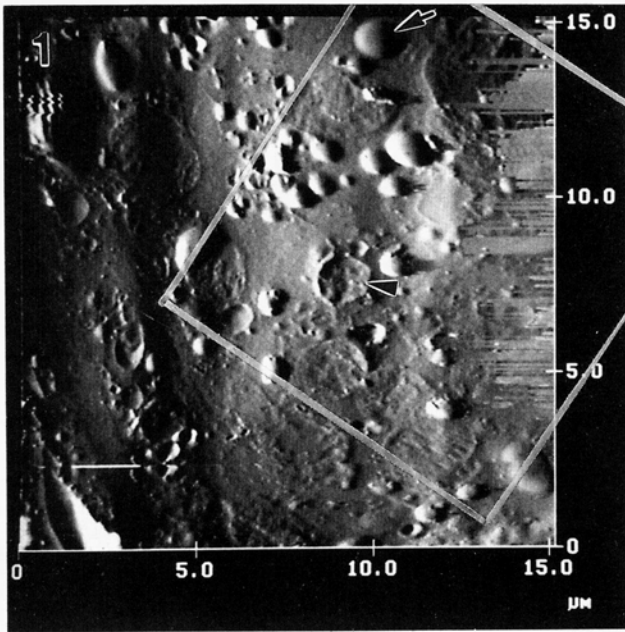
Fig. 1. Large scan area AFM error-mode image taken on side A showing the area from which the subsequent higher magnification images were taken (see Figs. 4, 5, 7–9). The box indicates the boundary of the stereo EM image shown in Fig. 2. In both Figs. 1 and 2 the arrow points to the same atrial granule, and the arrowhead to the same vesicular structure. Scale bar = 1 μm.

after the tip had passed, thereby obscuring certain features in the images taken on side A.

TEM and AFM images, obtained at comparable magnifications, of the same regions on the replica were mounted next to each other for comparison. Negative films of the stereo-pair photographs were examined at a magnification of 2×, as described previously (Kordylewski *et al.*, 1983, 1985). Selected EM images were reverse printed to make the shadows appear dark. Stereo images similar to those created from TEM were also created with AFM images using the AFM software by projecting two images viewed 5° apart. These stereo reconstructions were useful in distinguishing a bump from a depression and provided a better feeling for the 3-D nature of the surface. The apparent angle of 5° for the stereo images in EM and AFM was selected so as not to exaggerate or minimize the actual topography.

Results and discussion

Replicas of fractured faces examined by low-dose EM contained good quality areas of fractured atrial myocytes. Well-preserved cell nuclei, many atrial granules, mitochondria and myofilaments cross-fractured at various angles were all apparent. Membranes of nuclear envelopes and sarcolemma were clearly visible and showed many intramembranous particles on both P- and E-faces. Nuclear
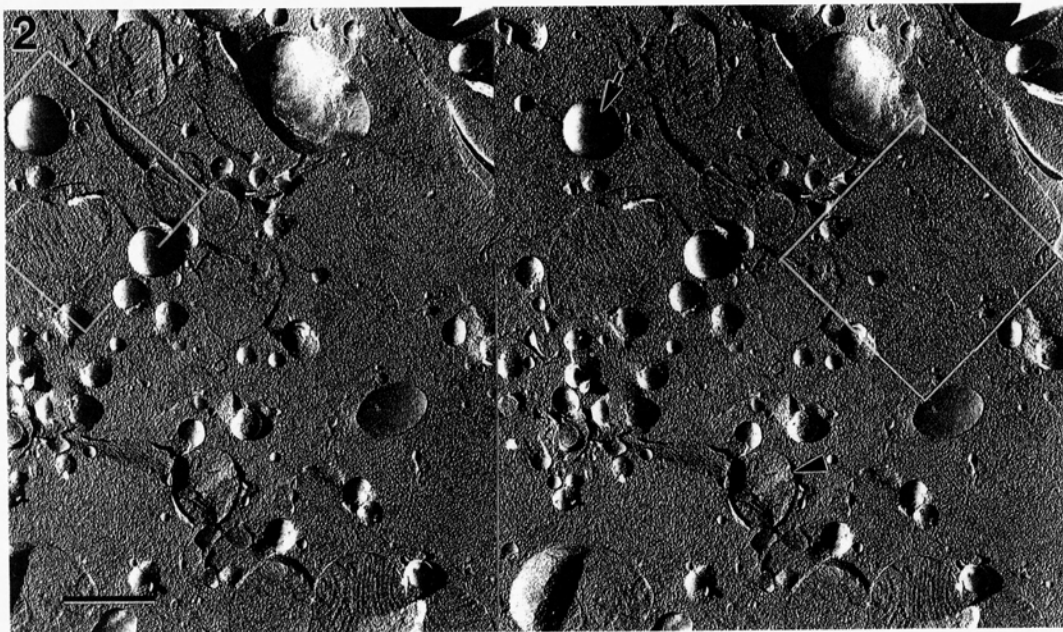

Fig. 2. TEM panaromic view of the area shown in detail in Figs. 3–9. The image is a stereo pair taken from a freeze-fractured replica of rat atrial tissue showing the myocyte interior with numerous atrial granules (regular spherical shapes), mitochondria (oval profiles) and other membranous vesicles densely covered with intramembrane particles. Most of the area shown is occupied by cross-fractured sarcoplasmic matrix, which displays granular texture, probably affected slightly by some ice formation. The somewhat regular pattern of the platinum grains is due to the presence of a regular network of myofilaments, which are, however, cross-fractured at various angles in different areas of the cell and are therefore not very distinct. The area shown in Fig. 3 is indicated by the box in the left image and that shown in Fig. 8 is indicated by the box in the right image. The arrow and arrowhead correspond to the arrow and arrowhead in Fig. 1. Scale bar = 1 μm.

pores were distinct, as were the cristae of the mitochondria. In AFM images, large features such as nuclei, atrial granules and large membrane patches were apparent and correlated well with the images obtained with TEM. On the other hand, smaller details were visible in AFM images of only one side of the replica.

Figures 1 and 2 show an AFM image and a low-magnification stereo TEM image of the same region of the replica, respectively. Several mitochondria and atrial granules were easily recognized. These structures were similar to those seen previously in identical freeze-fracture replicas (Page *et al.*, 1986; Kordylewski *et al.*, 1993).

Higher magnification images of the same region in the same replica, containing a mitochondrion and an atrial granule, are shown in Figs. 3–5. The mitochondrion with cristae (arrowhead) and the atrial granule (arrow) are clearly visible in the AFM image of side A of the replica (Fig. 4). The image taken on the other side (side B) of the replica is shown in Fig. 5. The boundary of the mitochondrion is discernible (arrowhead), but fine details such as cristae are not clear. We were able to locate the region on side B by aligning neighbouring larger structures
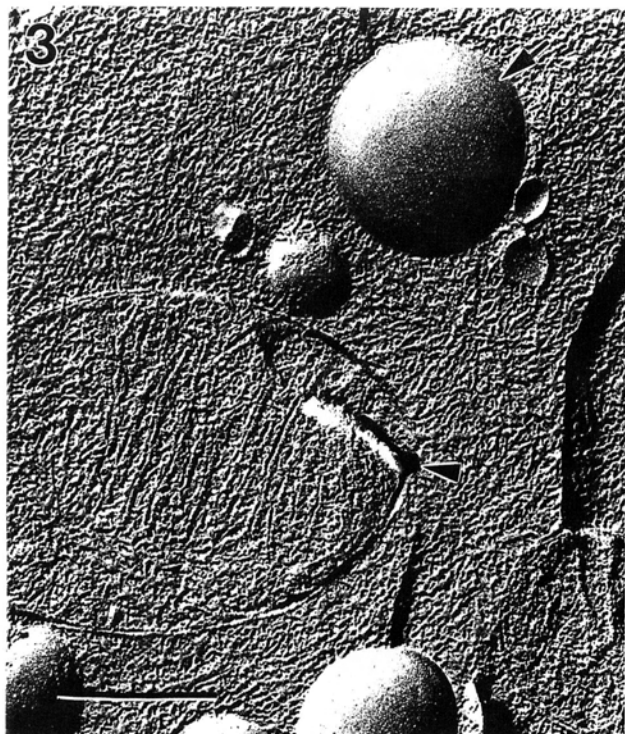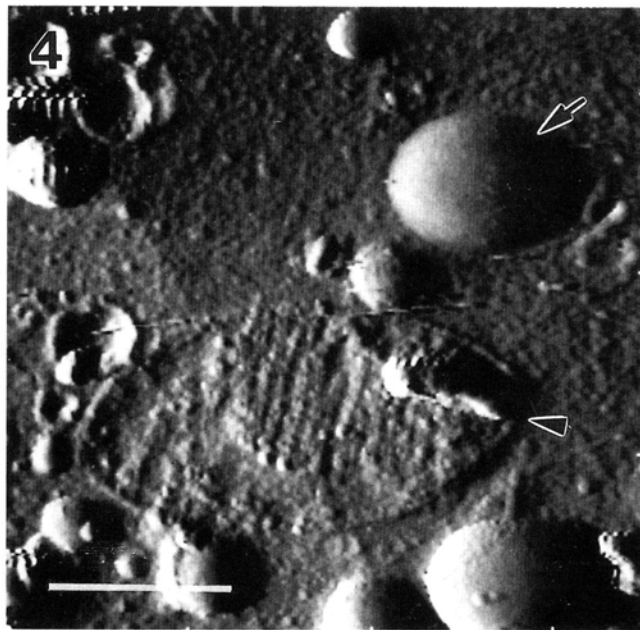

Fig. 4. AFM error-mode image of the region shown in Fig. 3 taken on side A of the specimen. Details in the mitochondrion as well as atrial granules and vesicles can be identified. The arrow and arrowhead point to the same features (atrial granule and mitochondrial chip, respectively) as the arrow and arrowhead shown in Figs. 3 and 5. Scale bar = 1 μm.

Fig. 3. Electron micrograph of the region of the replica shown in Fig. 2 and displayed at higher magnification. A mitochondrion, atrial granule (arrow) and small vesicles are visible. Mitochondrial membranes including distinct cristae are cross-fractured while the surfaces have been exposed in the atrial granules. Within the mitochondrion a small piece of the specimen has chipped off at the time of fracturing (arrowhead). Scale bar = 0·5 μm.
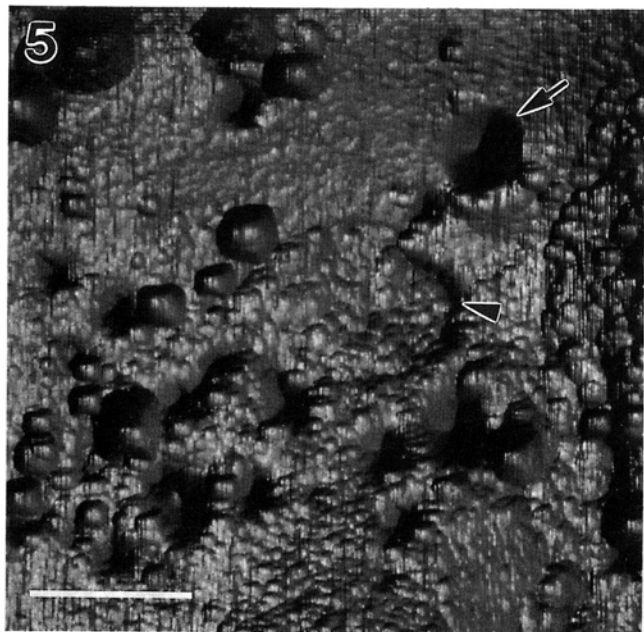

Fig. 5. Illuminated height-mode AFM image of the same region shown in Figs. 3 and 4 taken on side B of the specimen. For the sake of comparison with Figs. 3 and 4, the original image has been printed with the negative flipped over (reversed). (AFM images taken on opposite sides of the replicas are mirror images of each other.) The boundary of the mitochondrion is difficult to discern, and none of the details are visible on this side of the sample. Again, the arrow and arrowhead correspond to those in Figs. 3 and 4. Scale bar = 1 μm.
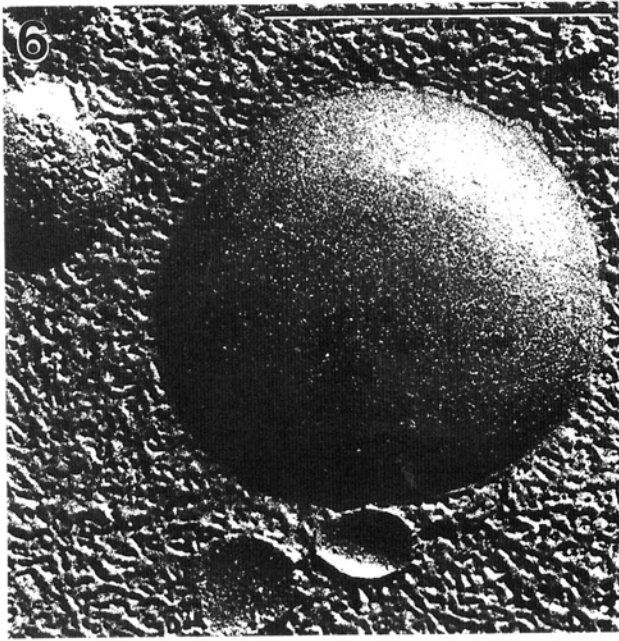
Fig. 6. Enlarged TEM view of the atrial granule shown in Figs. 1–5. The grains of platinum, which limit the resolution of the EM image, are clearly visible in both the rough area of the sarcoplasm surrounding the granule and on the rather smooth surface of the granule. Scale bar = 0·5 μm.
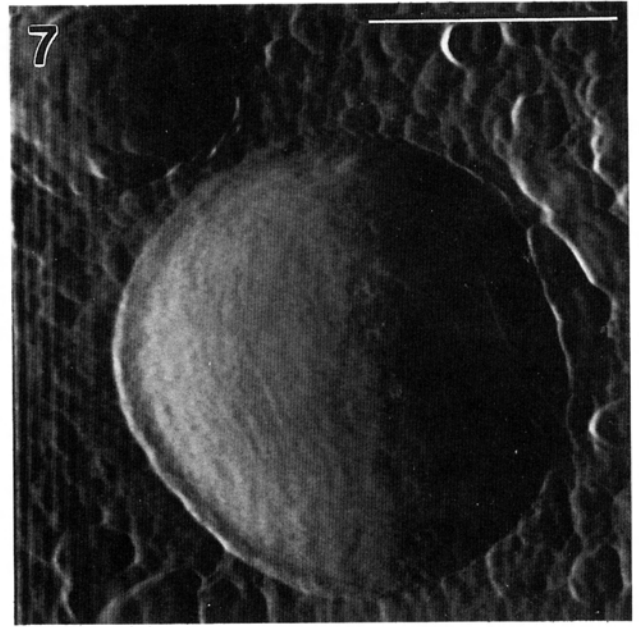
Fig. 7. AFM error-mode image taken from side A of the replica showing the same atrial granule shown in Fig. 6 and at a comparable magnification to Fig. 6. Note that the surface appears less granular than in Fig. 6. Scale bar = 0·5 μm.

with the TEM images. The same atrial granule (arrow) and the smaller bump next to the mitochondrion (arrowhead) are visible in AFM images from both sides of the replica. In both the TEM image (Fig. 3) and the AFM image from side A (Fig. 4), mitochondrial cristae are clearly visible and

correlate well. Also present in both of these images is a small 'chip' in the specimen, probably created during the fracture process (arrowhead). Using the off-line AFM software, the mitochondrion was measured at ~ 2·20 μm long and ~ 1·3 μm wide. These dimensions compare favourably with those taken from the TEM images
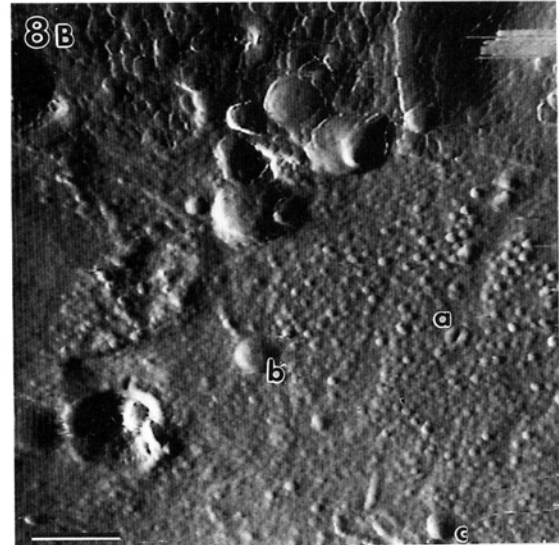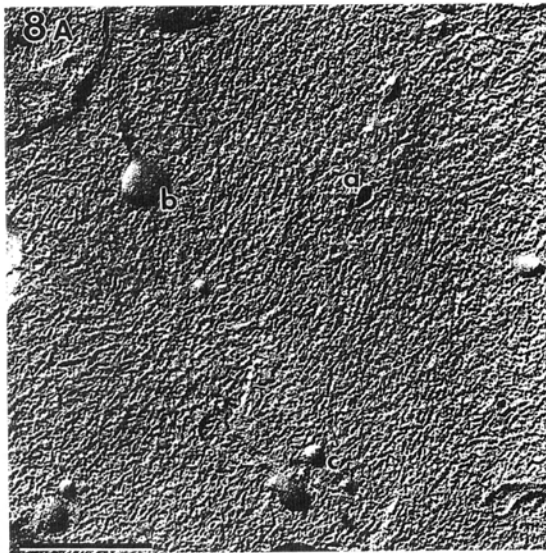

Fig. 8. Electron micrograph (A) of a region which was noticed to have an unusual surface texture while imaging by AFM. The AFM error-mode image (B) of the same region shows features (small circular bumps) not visible in the EM image. Letters (a, b and c) indicate corresponding vesicular features which served as landmarks for identification in the two images. Scale bars = 0·5 μm.
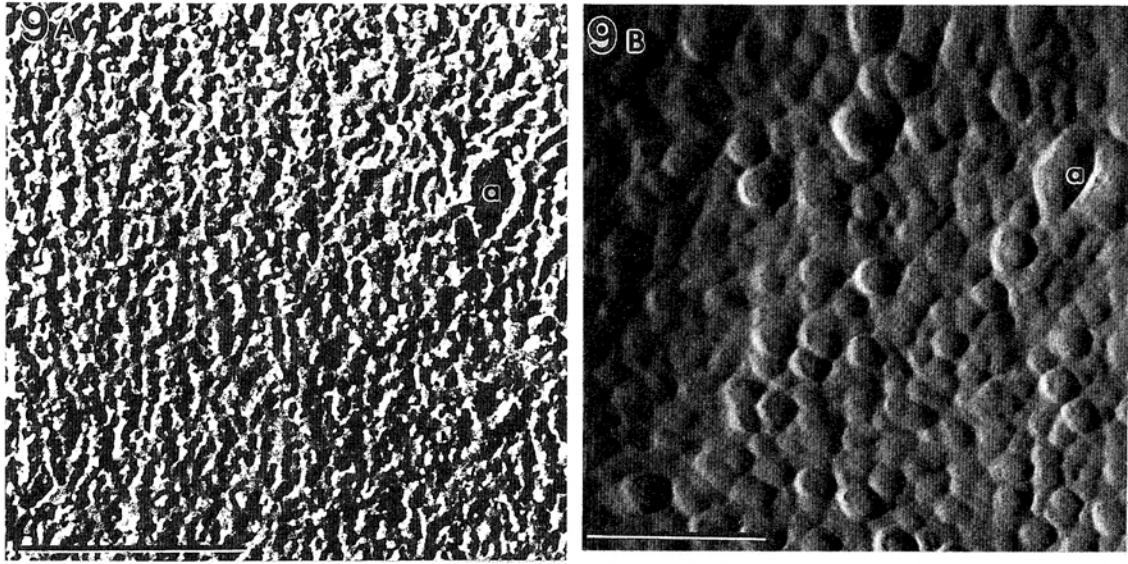
Fig. 9. High-magnification TEM image (A) and an AFM error-mode image (B) of a region displayed in Fig. 8 ('a' corresponds to the same vesicular structure in both Figs. 8 and 9). Note the disparity between the EM and AFM images; the regular pattern of bumps in the AFM image is not present in the EM image. Again, the AFM image was taken on side A of the sample. Scale bars $= 0.25\,\mu$m.

($\sim 1.8\,\mu$m and $\sim 1.1\,\mu$m, respectively), given an uncertainty of ~ 5–10% in AFM measurements.

Higher magnification images of the same atrial granule are shown in Figs. 6 and 7. Again the correlation between the AFM and TEM images is quite clear. AFM measurements

show the granule is $\sim 0.95\,\mu$m in diameter and $\sim 86\,$nm tall. This type of quantitative height measurement is not readily available with TEM.

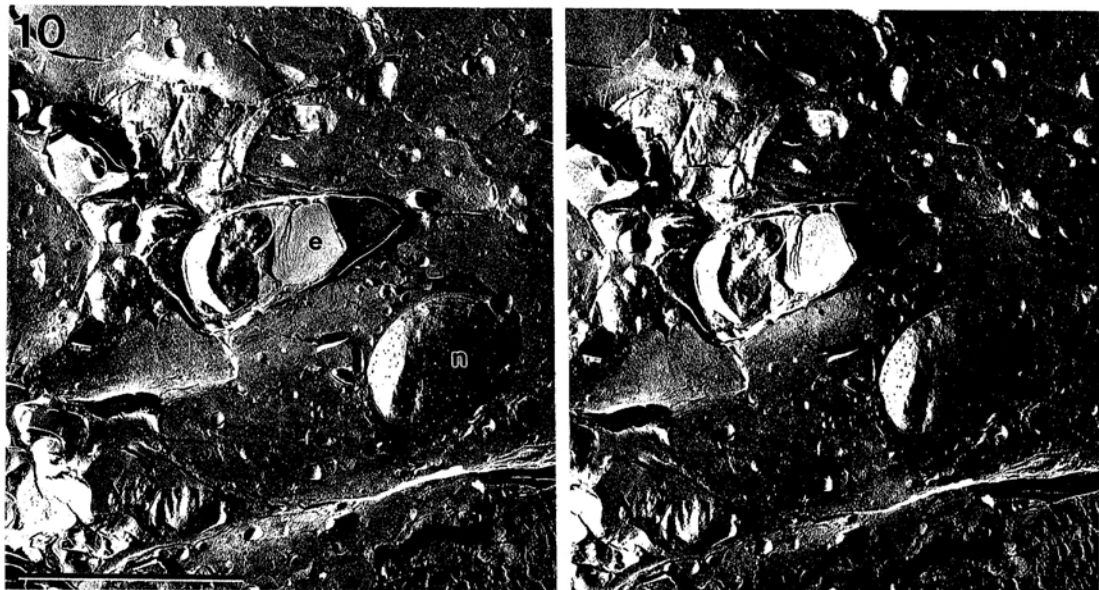A sequence of images at different magnifications is shown in Figs. 8 and 9. An unusual surface texture was noticed in

Fig. 10. Low-power TEM panoramic stereo view of the freeze-fractured replica. There are several cross-fractured myocytes in the viewing area. The large oval profile represents a cell nucleus (n) located in the centre of one of the myocytes. The fracture plane travelled across the sarcoplasm and then along the nuclear envelope causing the nucleus to bulge upward from the plane of the specimen. An enlarged view of this nucleus is shown in Fig. 12. The other prominent structure beside the nucleus is a capillary, cross-fractured open showing a broken erythrocyte (e) and a large patch of endothelial cell membrane with numerous caveolae. Scale bar $= 10\,\mu$m.
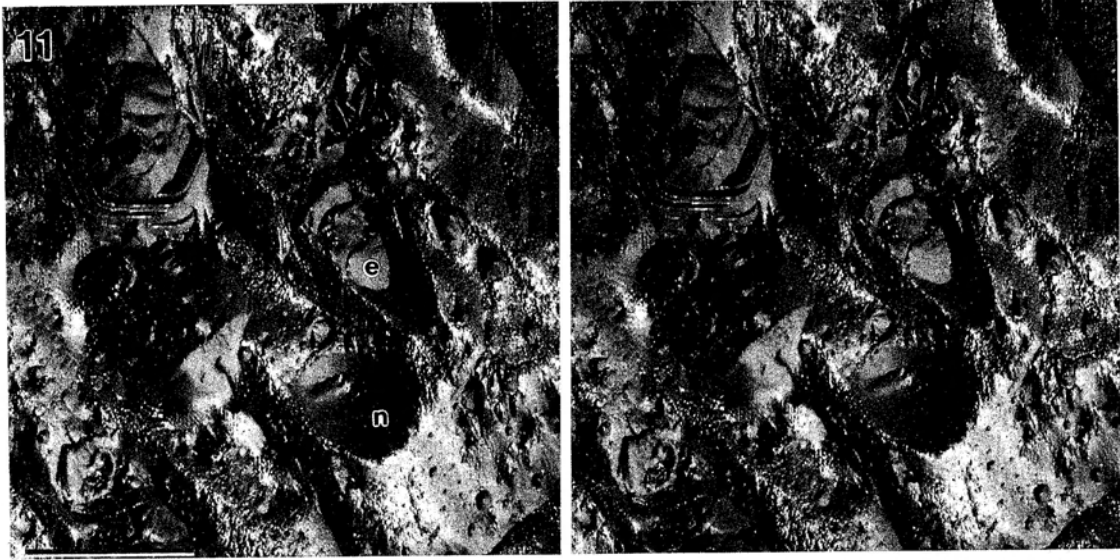
Fig. 11. AFM stereo view created from illuminated height-mode data taken on side B of the sample corresponding to the same area shown in Fig. 10. Clearly visible are the atrial cell nucleus (n) and the erythrocyte (e). This image is rotated ~ 90° with respect to the image presented in Fig. 10. Scale bar = 10 μm.

this region during AFM imaging of side A. The pattern visible in the AFM images (Figs. 8B, 9B) is quite distinct from the pattern present in the EM images of the same region (Figs. 8A, 9A). The small circular profiles in the AFM image (Fig. 9B) have a diameter of ~ 63 nm and a height of ~ 13 nm.

Whether such disparities between AFM and EM images are common needs to be studied further. Some unusual patterns were reported previously in high-magnification STM images of freeze-fracture replicas of artificial membranes (Zasadzinski *et al.*, 1988). The disparity in the AFM and TEM images is presumably a result of the difference in the nature of the image formation (3-D surface information in AFM versus 2-D projection of bulk image in TEM) and shows that perhaps new and different information can be obtained from examination of these samples with AFM.

Figures 10 and 11 show a low-magnification stereo EM image and the corresponding stereo AFM image (taken on side B) of a nucleus and cell membrane patches, respectively. The nucleus, which protrudes from the EM stereo image (n in Fig. 10), appears as a depression in the replica when viewed from side B by AFM (n in Fig. 11). This depression is ~ 1 μm deep, 6·65 μm long and 4·76 μm wide.

The higher magnification EM image (Fig. 12) and AFM images of both sides B and A (Figs. 13 and 14, respectively) of the same nucleus were analysed. In these images the nuclear pores are clearly visible, and fine details can be discerned from a zoomed AFM image (Fig. 14) of side A. From the EM image (Fig. 12) and the AFM image of side A (Fig. 14), it can be seen that some of the pores are blocked and some are open. In the AFM image of side B (Fig. 13), the

nuclear pores appear as protrusions (bumps) on the surface, while in the image of side A (Fig. 14), both protrusion and depression (holes) are visible. The pore diameter measured on side A (in the depression) was 80 ± 12 nm, which
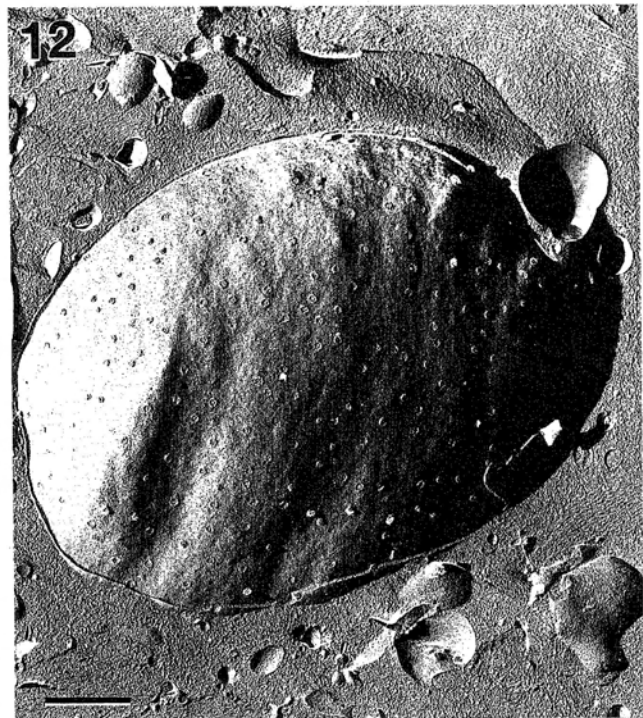

Fig. 12. High-magnification EM image of the nucleus shown in Figs. 10 and 11. Many nuclear pores are visible, some of which appear to be blocked. Scale bar = 1 μm.
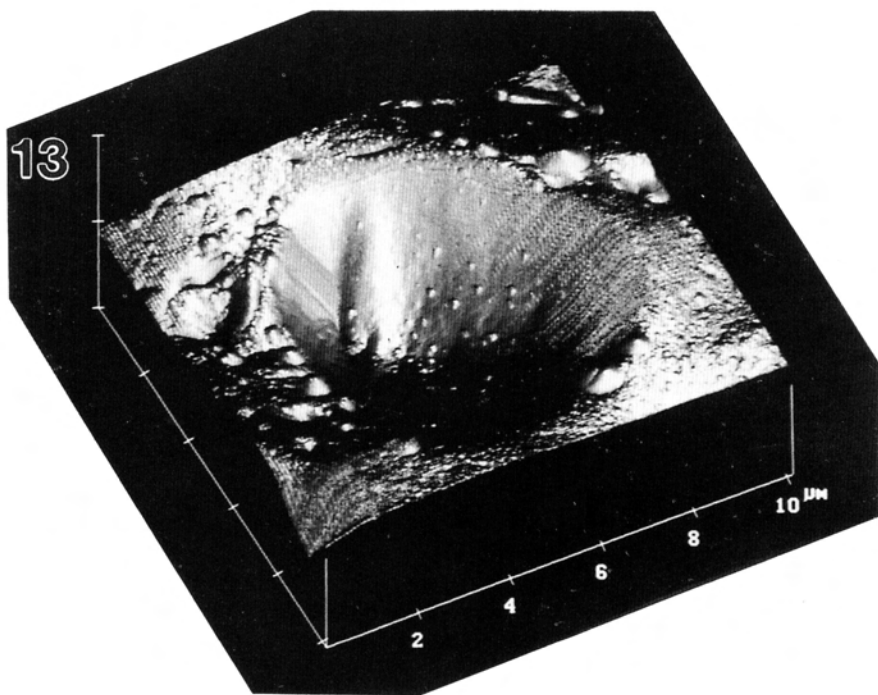
Fig. 13. High-magnification AFM surface plot of the nucleus presented in Figs. 10–12 taken on side B of the specimen. The surface plot illustrates the capacity of the AFM to obtain 3-D information from the surface. Again visible are several nuclear pores, some also appearing to be blocked and manifesting themselves as distinct bumps.

compares well with previously published dimensions of ∼ 75 nm (Roberts *et al.*, 1991). The pore diameter measured from the protrusion (side B) was considerably larger (∼ 125 nm) and may reflect a tip size effect. The depth in the centre of pores varied from 15 to 22 nm. These measurements could be an underestimation of the actual pore thickness across the membrane due to the pyramidal probe tips that could not penetrate all the way through the smaller diameter pores. Measurements of the dimensions of structural details in the replica, especially in the *z*-direction, could be made with the AFM software far more easily than on the EM stereo images with the photogrammetric method (Turner, 1981; Engel *et al.*, 1982; Kordylewski & Florek, 1990).
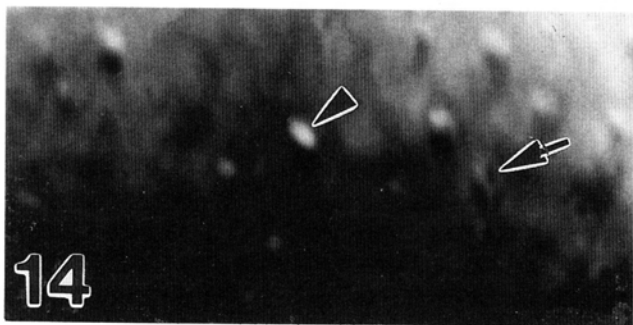
In summary, the results from this correlative study not only help verify AFM images, but also reveal new information about EM images of freeze-fractured replicas (surface-specific details, height of replica features). Also, this study points out the possibility of creating specimens which would be better suited for and could be examined directly by AFM. Since AFM can image surface topology directly, there should be no need for shadowing the sample with high-density particles (such as platinum). As the AFM technique develops further, it should be possible to obtain high-resolution surface images of native freeze-fractured biological specimens.

Acknowledgments

Fig. 14. Zoomed AFM error mode image taken on side A of the specimen showing nuclear pores (arrow points to an open pore, arrowhead points to a blocked pore). The pore diameters were measured to be ∼ 80 nm from this image.

References

Binnig, G., Quate, C.F. & Gerber, C. (1986) Atomic force microscope. *Phys. Rev. Lett.* **56**, 930–933.

Binnig, G. & Rohrer, H. (1982) Scanning tunneling microscopy. *Helv. Phys. Acta*, **55**, 726–735.

Butt, H.J., Downing, K.H. & Hansma, P.K. (1990) Imaging the membrane protein bacteriorhodopsin with the atomic force microscope. *Biophys. J.* **58**, 1473–1480.

Clemmer, C.R. & Beebe, T.P. (1991) Graphite: a mimic for DNA and other biomolecules in scanning tunneling microscope studies. *Science*, **251**, 640–642.

Engel, A. (1991) Biological applications of scanning probe microscopes. *Ann. Rev. Biophys. Biophys. Chem.* **20**, 79–108.

Engel, A.G., Fukunaga, H. & Osame, M. (1982) Stereometric estimation of the area of the freeze-fractured membrane. *Muscle and Nerve*, **5**, 682–685.

Hayat, M.A. (1987) *Correlative Microscopy In Biology*. Academic Press, London.

Heckl, W.M. & Binnig, G. (1992) Domain walls on graphite mimic DNA. *Ultramicroscopy*, **42**, 1073–1076.

Hoh, J.H., Lal, R., John, S.A., Revel, J.P. & Arnsdorf, M.H. (1991) Atomic force microscopy and dissection of gap junctions. *Science*, **253**, 1405–1408.

Hoppe, W. (1991) Three-dimensional electron microscopy. *Ann. Rev. Biophys. Bioeng.* **10**, 563–592.

Kordylewski, L. & Florek, R. (1990) Stereogrammetric measurements of cell membrane structures in freeze-fracture replicas. *First Regional Meeting of the American Society for Cell Biology, Program, Chicago*. p. 34. ASCB, Chicago.

Kordylewski, L., Goings, G.E. & Page, E. (1993) Rat atrial myocyte plasmalemmal caveolae *in situ*: reversible experimental increases in caveolar size and in surface density of caveolar necks. *Circ. Res.* **73**, 135–146.

Kordylewski, L., Karrison T. & Page, E. (1983) P-face particle density of freeze-fractured vertebrate cardiac plasma membrane. *Am. J. Physiol.* **248**, H992–H997.

Kordylewski, L., Karrison, T. & Page, E. (1985) Measurements on the internal structure of freeze-fractured cardiac plasma membrane. *Am. J. Physiol.* **248**, H297–H300.

Lal, R. & John, S.A. (1994) Biological applications of atomic force microscopy. *Am. J. Physiol. Cell Physiol.* **266**, C1–C21.

Lal, R., Kim, H., Garavito, R.M. & Arnsdorf, M.F. (1993) Molecular resolution imaging of reconstituted biological channels using atomic force microscopy. *Am. J. Physiol.* **265**, C851–C856.

Lal, R. & Yu, L. (1993) Atomic force microscopy of cloned nicotinic acetylcholine receptor expressed in *Xenopus* oocytes. *Proc. Natl Acad. Sci. USA*, **90**, 7280–7284.

Marti, O., Ribi, H.O., Quate, C.F., Drake, B., Albrecht, T.R. & Hansma, P.K. (1988) Atomic force microscopy of an organic monolayer. *Science*, **239**, 50–52.

Page, E., Goings, G.E., Power, B. & Upshaw-Earley, J. (1986) Ultrastructural features of atrial peptide secretion. *Am. J. Physiol.* **251**, H340–H348.

Pante, N. & Aebi, U. (1993) The nuclear pore complex. *J. Cell Biol.* **122**, 977–984.

Putnam, C.A.J., Van Der Werf, K.O., De Grooth, B., Van Hulst, N.F., Greve, J. & Hansma, P.K. (1992) A new imaging mode in atomic force microscopy based on the error signal. *SPIE: Scanning Probe Microscopies*, **1693**, 198–204.

Roberts, R.L., Kessel, R.G. & Tung, H. (1991) *Freeze-Fracture Images of Cells and Tissues*. Oxford University Press, Oxford.

Rugar, D. & Hansma, P. (1990) Atomic force microscopy. *Phys. Today*, **43**, 23–30.

Turner, J.N. (1981) Introduction to stereo imaging. *Methods in Cell Biology* (ed. by J.N. Turner), Vol. 22, *Three Dimensional Ultrastructure in Biology*. pp. 1–11. Academic Press, NY.

Yang, J., Tamm, L.K., Tillack, T.W. & Shao, Z. (1993) New approach for atomic force microscopy of membrane proteins—The imaging of cholera toxin. *J. Mol. Biol.* **229**, 286–290.

Zasadzinski, J.A.N. & Hansma, P.K. (1990) Scanning tunnelling microscopy and atomic force microscopy of biological surfaces. *Ann. NY Acad. Sci.* **589**, 476–491.

Zasadzinski, J.A.N., Schneir, J., Gurley, J., Elings, V. & Hansma, P.K. (1988) Scanning tunneling microscopy of replicas of biomembranes. *Science*, **239**, 1014–1016.